Molecular Bridges Link Monolayers of Hexagonal Boron Nitride during Dielectric Breakdown

ACS APPLIED ELECTRONIC MATERIALS

pubs.acs.org/acsaelm Article

Molecular Bridges Link Monolayers of Hexagonal Boron Nitride during Dielectric Breakdown

Alok Ranjan,* Sean J. O'Shea,* Andrea Padovani, Tong Su, Paolo La Torraca, Yee Sin Ang, Manveer Singh Munde, Chenhui Zhang, Xixiang Zhang, Michel Bosman, Nagarajan Raghavan, and Kin Leong Pey

Cite This: *ACS Appl. Electron. Mater.* 2023, 5, 1262−1276 Read Online

ACCESS | Metrics & More | Article Recommendations | Supporting Information

ABSTRACT: We use conduction atomic force microscopy (CAFM) to examine the soft breakdown of monocrystalline hexagonal boron nitride (h-BN) and relate the observations to the defect generation and dielectric degradation in the h-BN by charge transport simulations and density functional theory (DFT) calculations. A modified CAFM approach is adopted, whereby 500 × 500 nm^2 to 3 × 3 μm^2 sized metal/h-BN/metal capacitors are fabricated on 7 to 19 nm-thick h-BN crystal flakes and the CAFM tip is placed on top of the capacitor as an electrical probe. Current−voltage (*I-V*) sweeps and time-dependent dielectric breakdown measurements indicate that defects are generated gradually over time, leading to a progressive increase in current prior to dielectric breakdown. Typical leakage currents are around 0.3 A/cm^2 at a 10 MV/cm applied field. DFT calculations indicate that many types of defects could be generated and contribute to the leakage current. However, three defects created from adjacent boron and nitrogen monovacancies exhibit the lowest formation energy. These three defects form molecular bridges between two adjacent h-BN layers, which in turn "electrically shorts" the two layers at the defect location. Electrical shorting between layers is manifested in charge transport simulations, which show that the *I-V* data can only be correctly modeled by incorporating a decrease in effective electrical thickness of the h-BN as well as the usual increase in trap density, which, alone, cannot explain the experimental data. An alternative breakdown mechanism, namely, the physical removal of h-BN layers under soft breakdown, appears unlikely given the h-BN is mechanically confined by the electrodes and no change in AFM topography is observed after breakdown. High-resolution transmission electron microscope micrographs of the breakdown location show a highly localized (<1 nm) breakdown path extending between the two electrodes, with the h-BN layers fractured and disrupted, but not removed.

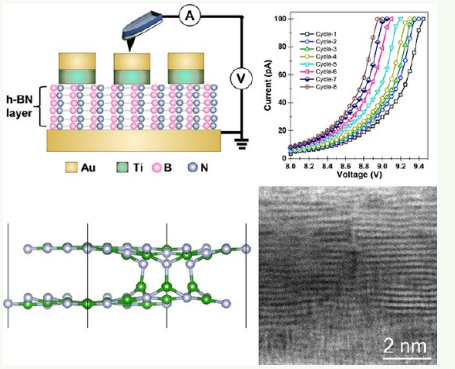

KEYWORDS: *conduction AFM, gate dielectric, h-BN, 2D layer breakdown, and reliability*

1. INTRODUCTION

Hexagonal boron nitride (h-BN) is a van der Waals layered material that has numerous potential applications.[1] In particular, h-BN has been very popular as a substrate for 2D semiconductor devices as it provides an atomically flat surface and an interface that is free of dangling bonds.[2] Recently, defects in h-BN have also become crucial to harness novel quantum phenomena, including realizing the brightest single photon sources.[3] Importantly, h-BN has also emerged as a key material to be used as a gate dielectric for 2D nanoelectronics.[4] Previous attempts toward integration of conventional gate dielectrics (e.g., SiO_2 and HfO_2) with 2D materials such as graphene and MoS_2 have proven to be challenging due to the high interfacial defect density between a 3D dielectric and a 2D semiconductor, which greatly reduces the intrinsic carrier mobility.[5] Alternate layered dielectrics including Bi_2SeO_5,[6] mica,[7] oxidized HfS_2,[8] and $MoTe_2$[9] have also been proposed and are now actively investigated, although h-BN remains by far the most studied 2D insulator.[4,10−12] As such, it is crucial to assess the wear out and reliability of h-BN[13] before the material can be considered for gate dielectric applications and over the past few years, there have been considerable efforts in this direction.[14−17]

Prior reliability studies on h-BN can be separated into two groups depending on the growth process used to produce the h-BN film, namely: (a) scalable techniques such as chemical vapor deposition (CVD)[14,16] and molecular beam epitaxy (MBE)[18] and (b) mechanical exfoliation from bulk crystalline h-BN,[10,12,19] yielding micron-sized single crystal flakes transferred onto a surface of interest. State-of-the-art CVD/MBE

Received: December 17, 2022
Accepted: January 27, 2023
Published: February 9, 2023

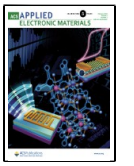

grown multi-layer h-BN films have poor thickness uniformity[14] and contain microstructural defects,[20,21] resulting in an unacceptably high leakage current and wide variability of electrical characteristics across devices. This renders CVD/MBE materials unsuitable for the study of intrinsic h-BN reliability and failure analysis. In contrast, with mechanical exfoliation, single crystalline h-BN flakes of uniform thickness can be routinely prepared from high-purity bulk crystals.[22] Although the lateral size of an exfoliated h-BN flake is typically only 10−50 μm, the defect density is 2−3 orders of magnitude lower than that of CVD/MBE h-BN,[23] thus providing a better platform to study the intrinsic material properties of h-BN and evaluate its suitability as a gate dielectric. In this work, we exclusively use exfoliated h-BN and our findings provide a benchmark to evaluate h-BN grown by the scalable CVD/MBE methods for practical future applications.

Charge transport measurements have shown that tunneling current depends exponentially on the number of h-BN layers[4,12] and direct tunneling is dominant for 1−3 layers. Intrinsic defects in h-BN act as quantum dots, modulating the local charge transport, and this effect is prominent in few layer-thick h-BN.[19] These pre-existing defects can also give rise to random telegraph noise,[24,25] ultimately leading to a drift of the transistor parameters (e.g., threshold voltage, drain current) over time. Noticeable Fermi level pinning was found at the metal/h-BN interface, suggesting a limited ability to control the band alignment.[26] Not surprisingly, the breakdown field strength (ξ_{BD}) in h-BN shows anisotropy,[15] with highest values reported along out-of-plane directions.

Most of the above charge transport measurements have been carried out using a metal/h-BN/metal crossbar test structure,[19,27,28] where the area of the resulting capacitor typically varies from 1 μm × 1 μm to 5 μm × 5 μm. The number of such crossbar capacitors, which can be fabricated on exfoliated h-BN flakes, is limited to around 10 per flake and hence only a limited set of capacitors is available for testing.[28] In this context, conduction atomic force microscopy (CAFM) has also been used to obtain complementary electrical data of exfoliated h-BN, with a movable sharp probe acting as the top electrode.[10] The area of contact largely depends on the radius of curvature of the AFM probe and typically varies between 10 and 100 nm^2, allowing large, statistically meaningful data sets to be collected on many single flakes. CAFM measurements have shown that the tunneling current distribution is highly uniform across a flake of fixed thickness[12] and the breakdown voltage is high and follows a Weibull distribution.[13]

Leakage current and breakdown voltage (or field strength) are two basic parameters essential for the characterization of gate dielectric reliability. However, to improve device performance and mitigate reliability issues, it is also critical to know the underlying atomic-scale mechanisms leading to degradation of the dielectric under an applied electrical stress. In this regard, there remain many open questions for h-BN related to defect generation, metal migration, and the evolution of the breakdown process. For example, the popular notation of 'layer-by-layer' breakdown in h-BN is often attributed to the physical fracture and subsequent removal of h-BN layers,[10] but importantly this is observed under hard breakdown (HBD), i.e., under conditions wherein a very high current flows and catastrophic material damage is to be expected. We have shown previously by CAFM that such mechanical damage is strongly suppressed in soft breakdown (SBD)[13,14] where the current is much lower. SBD represents a regime of more relevance with regard to circuit reliability as the integrated circuit chip remains functional although with reduced performance.[29,30] The influence of 2D layering can still be observed under SBD conditions in that current−voltage (*I-V*) curves measured by repeatedly ramping the voltage at one location often show (in ∼30% of the locations measured) a change in breakdown resistance corresponding to a change of one monolayer thickness between successive *I-V* ramps.[13] In this work, we attribute this to "electrical shorting" between layers rather than the physical removal of a h-BN layer. This interpretation is supported by our density functional theory (DFT) studies showing that atomic bonding between adjacent layers, which is referred to as "molecular bridging", can occur.[31] Our DFT study also showed many other types of defects that are stable and hence could be generated by electrical stress and contribute to the leakage current; a finding supported by our experimental observation that only ∼30% of the above mentioned CAFM *I-V* curves show electrical shorting of the h-BN layer behavior, with presumably the other 70% of the observations representing the effect of alternative defect configurations.[13] A recent extension of the DFT approach demonstrated that resistive switching in h-BN for use in memristor devices may also be based on the reversible formation of such molecular bridge defects, at least for the case studied involving tri-vacancy defects.[32] Importantly for our study, this work also showed that the electronic transmission function of the bridge-type defects is ∼1000× greater than that of pristine h-BN, indicating that a significant increase in charge transfer would occur through these bridge defects. Notwithstanding these insights, there remains uncertainty in the underlying atomistic mechanism responsible for stress-induced degradation of h-BN with regard to application in devices.

In this work, we combine experiments on capacitor test structures, charge transport simulations across the capacitors, and *ab initio* DFT calculations to gain robust insights into the defect generation, dielectric degradation, and breakdown in h-BN. We have designed a test methodology in which small capacitors, ranging from 500 × 500 nm^2 to 3 × 3 μm^2, are fabricated directly on a single crystal h-BN flake and a conducting AFM tip is brought into contact with the top capacitor electrode to carry out electrical measurements. We name this method Cap-AFM, and the approach circumvents several problems associated with traditional CAFM, such as the ill-defined area of the electrical junction, variability in the conductivity of the tip due to mechanical wear, and contamination of the tip apex while maintaining a sufficiently small junction area such that many capacitors can be microfabricated on a single h-BN flake for measurement. The Cap-AFM method is slower compared to standard CAFM because the AFM tip must be first aligned over the capacitor for the measurement. Nevertheless, a key advantage is that the method provides identical but more reproducible *I-V* data than CAFM, provided that the metal−dielectric interfaces are kept clean during the lithography processing. The smallest capacitors we have fabricated are 500 × 500 nm^2, which is a trade-off between having a large enough area to easily place the AFM tip and a small enough area to minimize the influence of extrinsic defects.

Our results show that defects are generated gradually over time and lead to a progressive increase in current prior to breakdown. Effects specifically arising from the 2D layering of h-BN, e.g., localized leakage current via a breakdown path, are

https://doi.org/10.1021/acsaelm.2c01736
ACS Appl. Electron. Mater. 2023, 5, 1262−1276

masked in electrical measurements on the capacitors because of the relatively large capacitor area, in contrast to our previous localized CAFM measurements. Despite this limitation, charge transport simulations and DFT calculations indicate that the data is best described by the continuous generation of defects, with the three lowest energy interlayer defect structures resulting in the formation of molecular bridges effectively leading to an "electrical shorting" between the h-BN layers. Further, physical removal of h-BN layers in the lead-up to breakdown does not appear likely as high-resolution transmission electron microscopy (TEM) cross-sectional analysis at the precise breakdown location shows a highly local breakdown path extending between the two electrodes, with the h-BN layers fractured and disrupted, but not removed.

2. RESULTS AND DISCUSSION

2.1. Test Structure and Physical Characterization. The test structures used consist of h-BN capacitors as shown schematically in Figure 1a. Two commonly used electrode

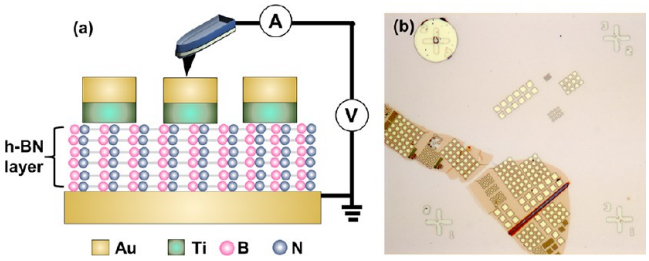

Figure 1. Experimental outline of Cap-AFM measurement. (a) Schematic showing the Au (bottom)/h-BN/Ti (top) capacitor test structure used in the experiments. h-BN is monocrystalline with thickness between 7 and 19 nm. The electrical connections for CAFM measurements used in the experiments are as shown. Bias is always applied to the CAFM tip, and the sample is electrically grounded. (b) Optical micrograph showing a 12 nm-thick h-BN flake on a Au-coated SiO_2/Si substrate after patterning the top electrode. The area of the capacitors varies from 500 nm × 500 nm to 3 μm × 3 μm.

materials (Au and Ti) are chosen for the bottom and top electrode, respectively. The h-BN is transferred using an all-dry transfer process, and details of the sample fabrication can be found in the Experimental Section. The thickness of the h-BN flakes vary between 7 and 19 nm, which is a useful range for gate dielectric applications in transistors. Electron beam lithography is used to pattern the top electrode, and the area of the electrode is varied between 500 nm × 500 nm to 3 μm × 3 μm squares, as shown in Figure 1b.

We use AFM to both image and electrically probe the fabricated h-BN capacitors. The tapping mode imaging is used to locate the capacitor, and CAFM is used to measure charge transport across the capacitor, as shown schematically in Figure 1a. We use Pt wire AFM cantilevers as these provide robust and reliable CAFM measurements. A semiconductor parameter analyzer is externally connected to the AFM, allowing the current flow to be limited to a set value at the instant of breakdown. This is an important consideration not only to protect the tip from high current induced damage, but also for dielectric breakdown measurements to enable the various stages of dielectric degradation to occur at different current injection levels. This gives access to stress-induced leakage current (SILC) at low current, SBD at moderate current, and HBD at high current.[33]

We use TEM to measure the thickness and crystallinity of h-BN in the as-prepared capacitors. A low-resolution overview of the cross section of a capacitor is shown in Figure 2a. A sacrificial layer consisting of SiO_x and Pt is deposited to prevent damage during focused ion beam (FIB) sample preparation. The TEM micrographs in Figure 2b,c show that the h-BN used in our experiments is monocrystalline and the as-fabricated devices do not contain any bulk structural defects, as commonly present in CVD-grown h-BN films. While the h-BN/metal interfaces are generally sharp, the top 1−3 layers (i.e., ∼1 nm) of h-BN near the Ti electrode have reduced crystallinity as shown in Figure 2d. We attribute this to process-induced damage caused by the electron-beam evaporation of the Ti contact, as also observed for other 2D materials.[34] A low-resolution cross-sectional TEM micrograph of a set of several capacitors fabricated on a 12 nm thick h-BN is shown in Figure S1. Analysis of this and similar TEM data show that the thickness of the h-BN is the same for different capacitors fabricated on the same flake, which is highly desirable for a quantitative analysis of charge transport and statistical analysis of variability across devices.

2.2. Charge Transport and Device-to-Device Variability. The dielectric breakdown field (ξ_{BD}) is one of the key metrics to evaluate any gate dielectric material, and we first measure it for the h-BN single crystals used in our experiments. Current−voltage breakdown curves for five different 500 × 500 nm^2 capacitors of a 12 nm-thick h-BN are shown in Figure 3a. The leakage current increases exponentially with applied bias and an abrupt increase in the leakage current is observed at the instant of SBD at ∼10 nA. We define the breakdown voltage (V_{BD}) as the voltage at which the current compliance is reached, e.g., 100 nA in Figure 3a, which is sufficiently high for SBD to occur, but far lower than typical HBD conditions, e.g., >1 μA for the 12 nm-thick flake of Figure 3a. The relation V_{BD}/t_{h-BN} is then used to obtain ξ_{BD}, where $t_{h\text{-}BN}$ is the flake thickness as measured by either AFM or TEM. Analysis across 5 different capacitors shows that ξ_{BD} is ∼15.8 ± 0.5 MV/cm for 12 nm-thick h-BN, comparable with the highest quality single crystalline h-BN reported to date.[27]

In general, we find that *I-V* curves show good uniformity for a fixed capacitor area but some variability is observed across h-BN flakes of different thicknesses. This result is summarized in Figure 3b,c, which shows the scaling of leakage current as a function of capacitor area and h-BN thickness. The current density at a fixed electric field (ξ) of 10 MV/cm for three different capacitor areas of 1 × 1 μm^2, 2 × 2 μm^2, and 3 × 3 μm^2 on a single 12 nm-thick flake is shown in Figure 3b. The current density (J) is moderately uniform (J within ∼40%) across the capacitors, with the smaller 1 × 1 μm^2 capacitors showing noticeably lower leakage current. There is greater variability in the current density as a function of h-BN thickness (J varies by ∼70%), as shown in Figure 3c. The *I-V* data are measured across different h-BN flakes of 12, 15, and 19 nm thicknesses for 2 × 2 μm^2 area capacitors and the current density for all three h-BN thickness are extracted at ξ = 10 MV/cm for comparison. It must be emphasized that relatively few capacitors are tested for each experimental condition and the sole purpose of Figure 3b,c is to provide a qualitative perspective of the data variability.

Charge transport simulations can be used to model the *I-V* electrical characteristics and extract useful data. Herein, we use a multi-phonon trap-assisted tunneling (MPTAT) description of the transport process[35,36] within the Ginestra simulation

https://doi.org/10.1021/acsaelm.2c01736
ACS Appl. Electron. Mater. 2023, 5, 1262−1276

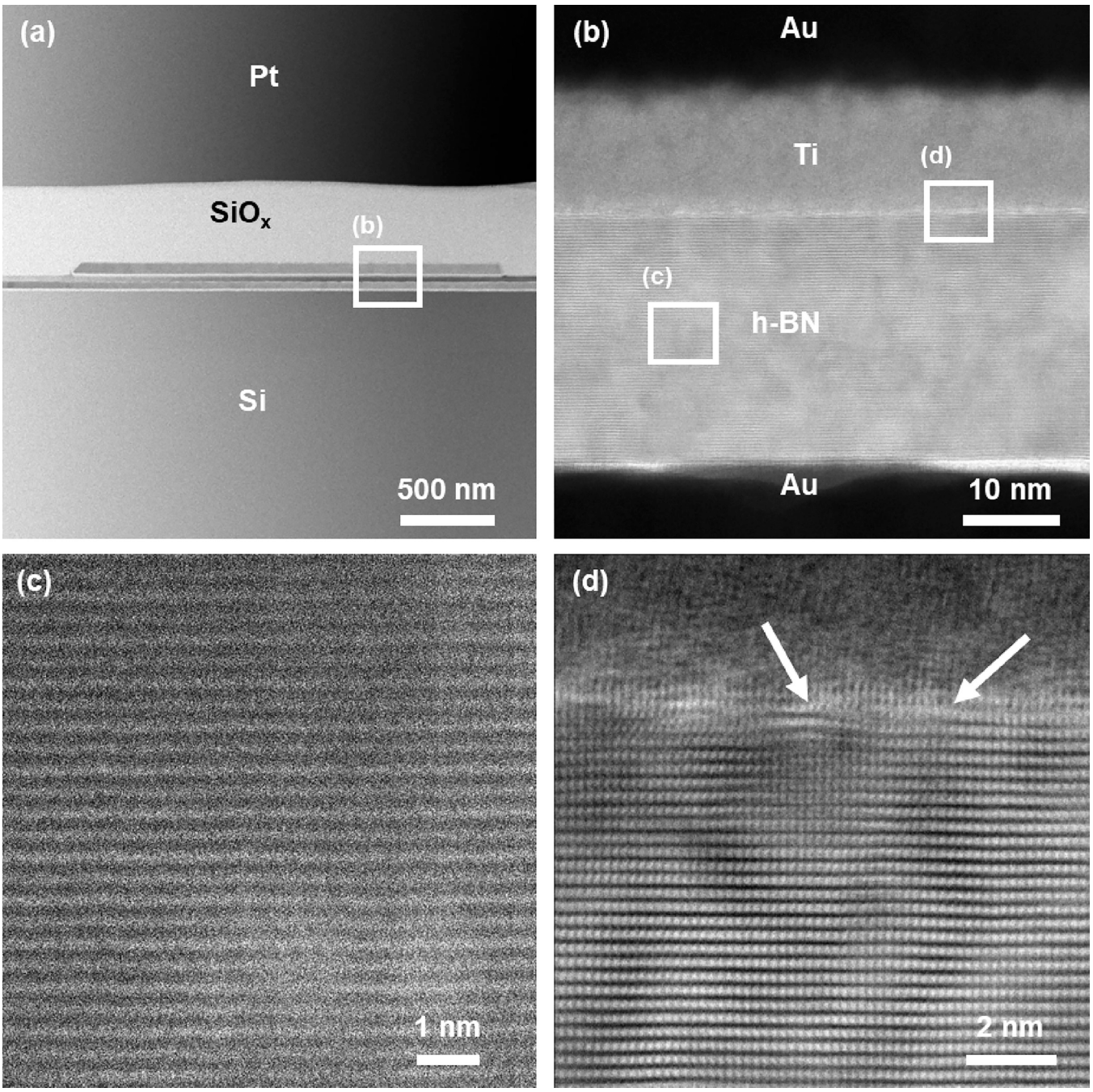

Figure 2. TEM micrographs of the as-prepared h-BN. (a) Low-resolution TEM micrograph showing the cross section of a capacitor. SiO_x and Pt layers were deposited to prevent damage to the capacitor during FIB sample preparations. (b) TEM micrograph showing a cross section of an as-prepared Au/h-BN/Ti capacitor taken at the location indicated by the square in panel (a). (c) High-resolution T EM micrograph from the bulk region of h-BN, indicated by the square in panel (b), showing the 2D layered structure. No obvious structural defects are visible. (d) TEM micrograph of the Ti/h-BN interface, indicated by the square in panel (b), where process-induced damage is observed in the top 1−3 layers of h-BN.

platform[37] to fit the experimental J-ξ data for different thicknesses (e.g., as shown in Figure S2), from which the trap energy (E_t) and trap density (N_t) can be extracted. Ginestra is a multiscale defect-centric simulation program, which self-consistently describes all the possible degradation mechanisms for dielectrics. Further details can be found in the Experimental Section and in previously reported works.[35,36] Within our simulation framework, traps are electrically active defects treated as discrete point entities that can trap and emit carriers and support their transport through the material. The number of traps within the considered material is determined by N_t that, together with their thermal ionization and relaxation energy distribution, determines the magnitude of the trap-assisted current as well as its dependence on the voltage (that is, the shape of the I-V curve). We find the experimental J-ξ data prior to any SBD event can be nicely reproduced in the simulation for different h-BN thicknesses by incorporating the parameters shown in Table S1, which are calculated by averaging over all the J-ξ data for a given thickness. Ginestra fitting for the 7 and 12 nm films shows that

https://doi.org/10.1021/acsaelm.2c01736
ACS Appl. Electron. Mater. 2023, 5, 1262−1276

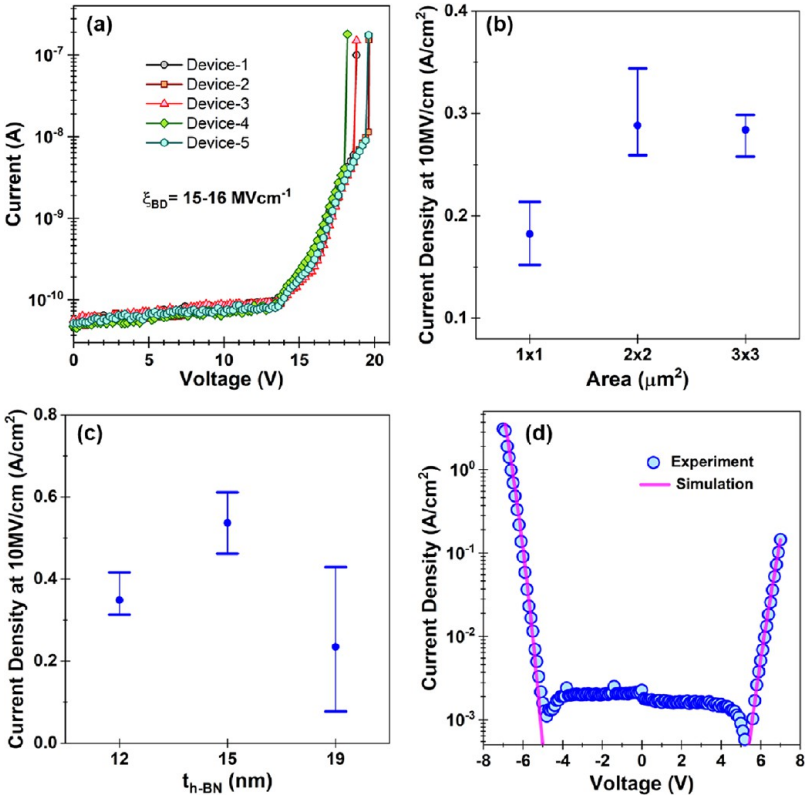

Figure 3. Cap-CAFM electrical measurements on h-BN capacitors. (a) *I-V* breakdown data measured across 5 capacitors on the same 12 nm-thick flake shows a breakdown field of 15−16 MV/cm. The area of the capacitors is 500 × 500 nm^2. (b) Plot showing the current density at 10 MV/cm for three different capacitor areas of 1 × 1 μm^2, 2 × 2 μm^2, and 3 × 3 μm^2 on 12 nm-thick h-BN. The number of capacitors tested for 1 × 1 μm^2, 2 × 2 μm^2, and 3 × 3 μm^2 are 8, 9, and 3, respectively. The error bars indicate the range of values measured. (c) Plot showing the current density for 2 × 2 μm^2 area capacitors as a function of h-BN thickness at a measured electric field of 10 MV/cm. The number of capacitors tested for 12, 15, and 19 nm thickness are 9, 4, and 4, respectively. The error bars indicate the range of values measured. Complete data sets for other capacitor sizes are plotted in Figure S2. (d) Plot of current density vs applied voltage for both positive and negative polarities on 7 nm-thick h-BN shows that the leakage current depends on the electrode used for current injection. Dots represent the experimental data while lines are Ginestra simulation fittings. The extracted values of work function for Ti and Au are 4.37 and 5.30 eV, respectively.

the average trap density in the h-BN crystal varies between 2 × 10^{17} and 4 × 10^{17} cm^{-3}. These defects in h-BN are located at the middle of the band gap, around 2.5 to 3.0 eV from the bottom edge of the conduction band.

We now discuss the role of the Au and Ti electrodes on the current injection. A representative *J*-ξ plot for 7 nm-thick h-BN for both positive and negative polarities is shown in Figure 3d. The measured current density is an order of magnitude higher for the same applied bias in the case of electron injection from Ti (at negative polarity) compared to Au. Ginestra simulation fittings to the experimental data show that the work functions of Au and Ti electrodes are 5.30 and 4.37 eV, respectively, in agreement with the previously reported values. We attribute the higher current injection from Ti at negative polarity primarily to its lower work function compared to Au, although effects from the defective Ti/h-BN interface cannot be ruled out.

2.3. Degradation and Dielectric Breakdown. In this section, we present the results on the defect generation, degradation, and dielectric breakdown in h-BN crystals by combining electrical measurements, *ab initio* DFT calculations, and physiochemical analysis using TEM.

2.3.1. Time-Dependent Dielectric Breakdown. Time-dependent dielectric breakdown (TDDB) measurements are standard reliability tests, which are useful to understand the temporal evolution of defects in a dielectric under an applied electrical stress.[38] The measurements are undertaken by applying a constant voltage stress (CVS), and the corresponding leakage current is monitored as a function of time. The choice of electric field/voltage is rather arbitrary and is chosen so that the measurement finishes within a reasonable time, typically ~10^2−10^3 s. TDDB data for five different 2 × 2 μm^2 capacitors measured at ξ = 8 MV/cm on 12 nm-thick h-BN are plotted in Figure 4a. The leakage current increases progressively with time until dielectric breakdown when the current increases abruptly by almost two orders of magnitude. These TDDB trends are consistent across all the devices, again indicative of the material homogeneity across a single h-BN crystal. The general features of TDDB in h-BN are similar to conventional dielectrics such as SiO_2 and HfO_2, with various stages of dielectric degradation clearly identified.[39] The first stage of TDDB shows charge trapping where pre-existing defects in the h-BN get filled and the tunneling current reduces to ~20% of the initial value. Following this, a SILC stage begins, characterized by the generation of new defects, which on further stressing, give rise to an increase in leakage current. Lastly, SBD occurs and the current increases abruptly to the current limit. It is important to highlight that charge trapping in h-BN is due to pre-existing defects in the crystal before any stressing. Both charge trapping and SILC components can be separated from the TDDB data, and the different charge transport mechanisms were analyzed individually.

https://doi.org/10.1021/acsaelm.2c01736
ACS Appl. Electron. Mater. 2023, 5, 1262−1276

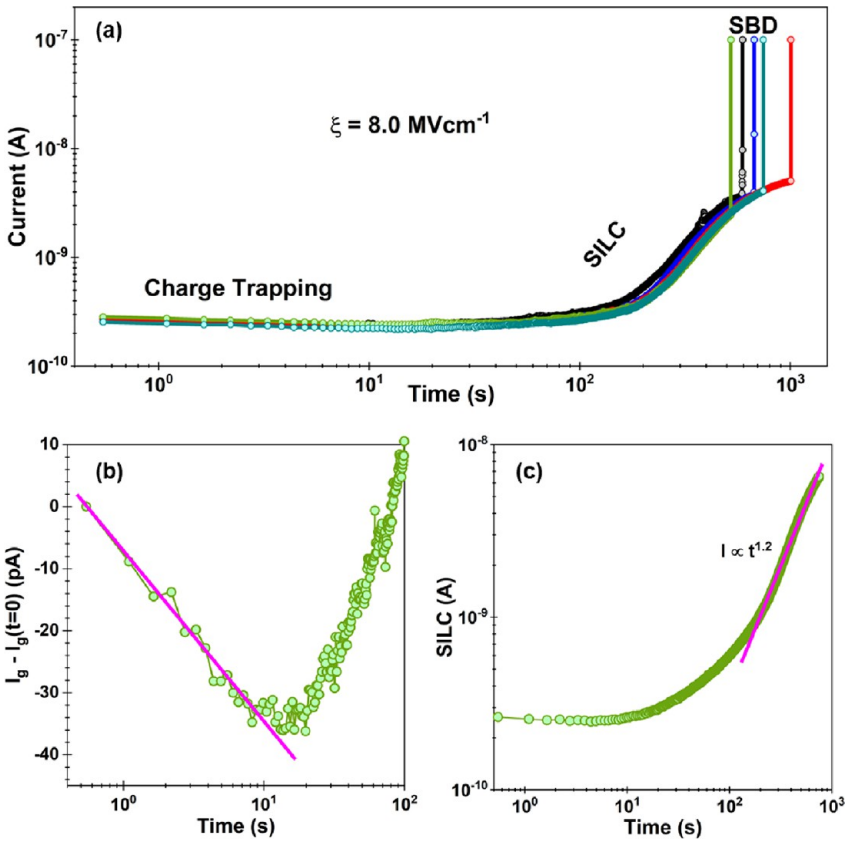

Figure 4. Cap-AFM measurement of TDDB characteristics of h-BN capacitors of 12 nm thickness. (a) TDDB data for five capacitors, each of area 2 μm × 2 μm, are plotted to show the TDDB trends. A compliance current of 100 nA is used. The leakage current increases progressively with time and various stages of TDDB can be identified including charge trapping, SILC, and SBD. (b) Zoomed-in view of the charge trapping regime highlighting the initial reduction in leakage current due to charge trapping at pre-existing defects in h-BN. The solid line (pink) is the linear fit of the decreasing part of the TDDB, which can be subtracted from the overall current shown in panel (a) to extract the SILC component. (c) Plot of the SILC component shows a progressive increase in current over time. Fitting shows that after the initial rise, the SILC current follows a power law $I \propto t^{\alpha}$ with exponent $\alpha \sim 1.2$ (solid pink line).

Following Degraeve *et al.*,[40] the charge trapping component is best represented by subtracting the TDDB current at time zero from the overall TDDB data, as plotted in Figure 4b. The charge trapping component decreases linearly with time and is modeled by a linear fit to the decreasing part of the current, as shown in Figure 4b by the solid line. This fitting is extrapolated to breakdown over the SILC stage and the value of the current subtracted from the TDDB data to yield the SILC component, as shown in Figure 4c. The SILC component follows a power law:[40]

$$I_{SILC} \propto t^{\alpha}$$

where I_{SILC} is the SILC current, t is the stress time, and α is the power law exponent. Typically, α depends on the applied electric field, temperature, and the dielectric material. In the initial phase of SILC (up to ~200 s), α is small and variable, suggesting a relatively slow generation of defects, which subsequently increases by an order of magnitude at the later stage to $\alpha = 1.2$. This general SILC behavior is similar to that observed in conventional oxides, e.g., in 10 nm-thick HfO_2 films and HfO_2/SiO_2 stacks with $\alpha \sim 1$.[41,42]

2.3.2. Layer Shorting Effect in h-BN. The defect generation rate in gate dielectrics depends on many experimental parameters, including applied electric field, current density (i.e., charge fluence), temperature, and current compliance (I_{comp}). We focus here on the effect of current compliance by using two I_{comp} values of 100 pA and 100 nA. In these experiments, a h-BN capacitor is subjected to repeated ramp voltage stress (RVS) at a ramp rate of 60 mV/s and the resulting *I-V* data are recorded to monitor the degradation trends. The *I-V* data for one such 2 × 2 μm^2 capacitor of 12 nm h-BN thickness subjected to I_{comp} = 100 nA is shown in Figure 5a,b. Repeated RVS leads to a progressive decrease in resistivity and eventually complete dielectric breakdown. This behavior is consistently observed across all capacitors, as shown in Figure S3. We use Ginestra to model all the *I-V* curves shown in Figure 5b and Figure S3, with symbols representing experimental data and solids lines the Ginestra simulation fittings. The major inference from the simulation is that changes in the trap density alone cannot account for the observed increase in the current during each RVS cycle, as to do so requires changing material parameters for each different *I-V*, which is not logical. We find the experimental RVS data can only be reproduced in a consistent way when both effective thickness and trap density are allowed to change simultaneously, as shown in Figure 5b, Figure S3, and Table S2. Here, the effective thickness is the "equivalent thickness" of h-BN that would give rise to the observed change in the current. For example, in fitting Figure 5b, the effective h-BN thickness reduces by 3.0, 2.5, 1.5, and 1.0 Å after the 1st, 2nd, 3rd, and 4th RVS stress cycles, respectively. Similar results are found on other thickness flakes, and Figure S4 and Table S3 show the

https://doi.org/10.1021/acsaelm.2c01736
ACS Appl. Electron. Mater. 2023, 5, 1262−1276

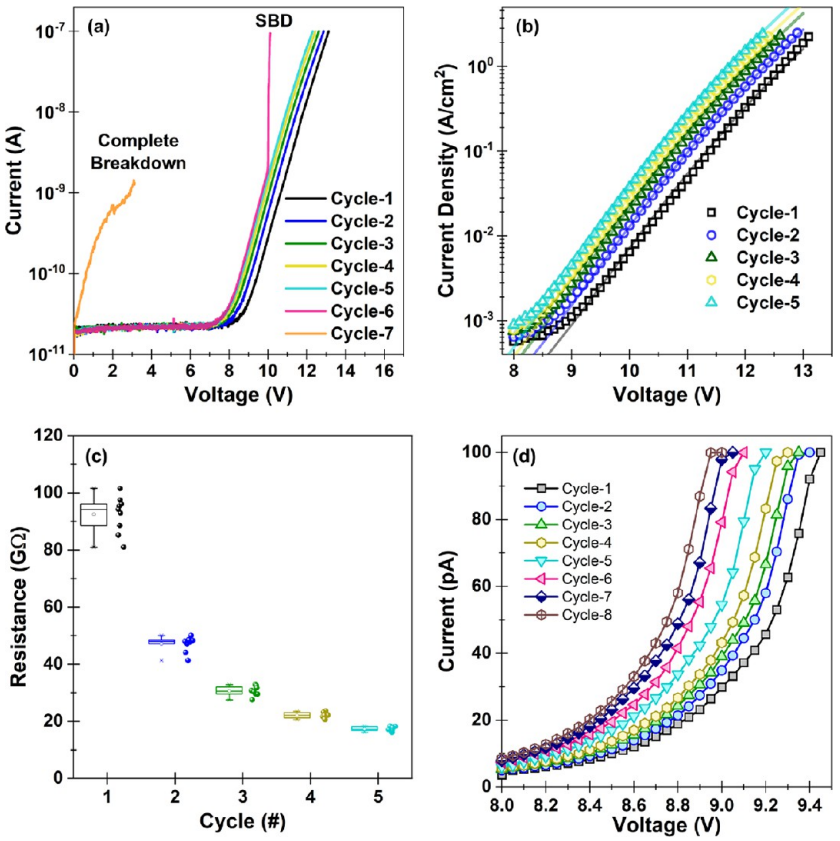

Figure 5. Cyclic ramp voltage stressing (RVS) by Cap-AFM of capacitors of 12 nm thickness. (a) *I-V* characteristics measured on a 2 × 2 μm^2 capacitor during repeated RVS stressing at compliance I_{comp} = 100 nA and ramp rate of 0.06 V/s. The data shows a gradual increase in the leakage current with successive RVS cycles and soft breakdown occurs at cycle 6. Note that the leakage current is higher here compared to the data in Figure 3a as the device area is larger. (b) Data (symbols) replotted for comparison with Ginestra charge transport calculations (solid lines). The simulation results only fit well with experimental data when an effective h-BN thickness reduction is also considered. (c) Plot showing the resistance of a capacitor decreasing with each RVS cycle. The resistance is extracted at an arbitrarily chosen bias of 9.50 V for each RVS cycle. The data is taken at I_{comp} = 100 nA over nine 2 × 2 μm^2 capacitors. (d) *I-V* plot measured on a 1 × 1 μm^2 capacitor during repeated RVS stressing at a low compliance of I_{comp} = 100 pA.

data for a 7 nm-thick flake. Note that each individual *I-V* is fitted (no averaging is undertaken) and importantly, the same material parameters are used to model both the 7 and 12 nm-thick RVS results.

The changes in the effective thickness in the above example are close to the monolayer thickness of h-BN (3.3 Å) and it would be tempting to infer that the reduction in thickness represents the breakdown of approximately one monolayer under each stress cycle. This is not the case, however, for the reasons now discussed. It is shown in Section 2.3.5 below that a type of defect referred to as a molecular bridge[31] most readily forms between two adjacent h-BN layers and will lead to high electron transmission, i.e., a low resistance path, between the two layers. This effect, which we also call "electrical shorting" between layers, can be observed directly by conduction AFM[13] because CAFM measures over an area of ∼10 × 10 nm^2 and hence a change in only a single h-BN layer greatly changes the out-of-plane resistance. In contrast, the current in a capacitor flows through a far larger area and the effect from the formation of a single molecular bridge defect is masked by the large leakage current. Similarly, for the TDDB data of Figure 4a, except the large increase in current when the stack undergoes SBD, there are no sudden jumps in conductivity that could be associated with the breakdown of individual h-BN layers. Rudimentary calculations assuming a 1 × 1 μm^2 capacitor made up of 10 × 10 nm^2 sized resistor elements in parallel, with resistance per layer given by the measured tunnel resistance of h-BN[12], indicate that the total resistance of the capacitor stack will only change by a small fraction (≪1%) if a single layer short-circuits in one of the resistive paths. Clearly, the resistance change between RVS cycles in Figure 5a is much larger, as shown explicitly in Figure 5b where the resistance is calculated at an arbitrarily chosen bias of 9.5 V for several 12 nm-thick capacitors. The resistance decreases to ∼50% of the initial value after the first cycle and subsequent RVS cycles lead to smaller but significant reductions of 10−20%.

Given that *I-V* data alone cannot provide unequivocal evidence about the nature or number of isolated defects, how can the RVS breakdown data taken on capacitors be interpreted? We postulate that the RVS data such as shown in Figure 5a represents the combined effect of in-plane and out-of-plane defects, but a significant component must be electrical shorting between layers by the formation of out-of-plane molecular bridges. Support for this interpretation comes from the Ginestra simulations, DFT calculations, and previous CAFM results.[13] The charge transport simulations show that the RVS data can only be well fitted by incorporating a change in effective thickness, leading to the conclusion that this thickness change represents the combined effect of many

https://doi.org/10.1021/acsaelm.2c01736
ACS Appl. Electron. Mater. 2023, 5, 1262−1276

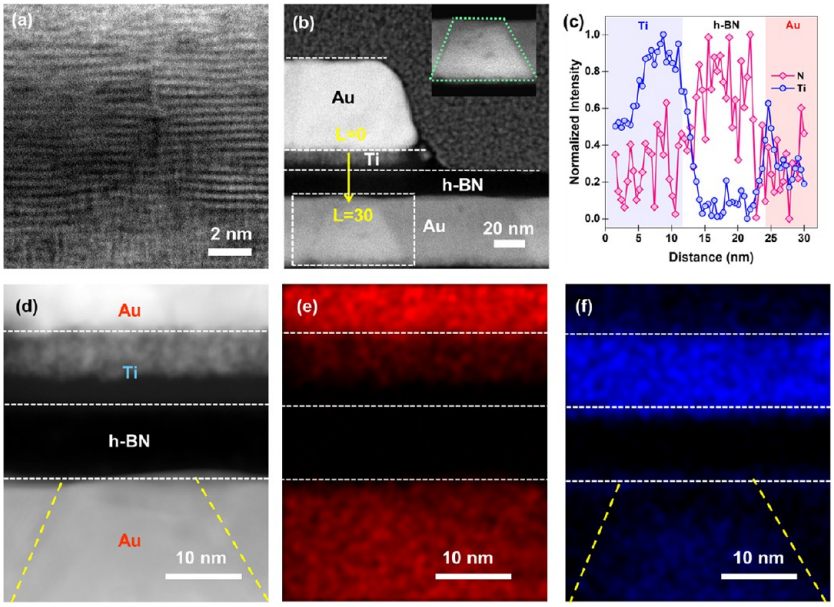

Figure 6. TEM data of electrically stressed capacitor. (a) HRTEM micrograph of a 10 nm-thick h-BN capacitor showing the h-BN layers after dielectric breakdown. The image shows the breakdown spot induced by an SBD event. The crystallinity of the h-BN is severely disrupted after breakdown as compared to unstressed h-BN, e.g., as shown in Figure 2c. The area of the capacitor is 500 nm × 500 nm, and the breakdown compliance is I_{comp} = 100 nA. (b) HAADF STEM micrograph showing the cross section of the stressed device where a material change in the shape of a truncated cone (marked by dotted lines) is visible at the bottom Au electrode. A zoomed-in view of the truncated cone is shown in the inset at upper right. (c) EELS analysis across the line shown as L = 0 to L = 30 nm in panel (b) showing the elemental distribution of Ti and N. A significant migration of Ti occurs from the top to the bottom electrode. (d) High-resolution STEM micrograph showing the zoomed-in view of the truncated cone site, highlighted at the bottom Au electrode by the dashed lines. (e) EDX elemental map of Au and (f) Ti for the area shown in panel (d). EDX analysis confirms the migration of Ti to the bottom electrode after breakdown.

different locations within the stack experiencing localized electrical shorting between h-BN layers.

Evidence showing that adjacent layers can indeed form electrical shorts under electrical stress is provided by our previous CAFM experiments in which it was observed that ∼30% of the RVS curves[13] showed discrete changes in the *I-V*. As noted above, since CAFM is a highly localized measurement over an area of approximately 10 × 10 nm^2, the discrete changes in *I-V* could be confidently associated with the localized breakdown of one or two monolayers of h-BN. Finally, DFT results described in Section 2.3.5 below and by others[31] show that many different types of stable defects can be generated in h-BN, both in-plane and out-of-plane. Significantly, a set of defects formed by molecular bridges between layers exhibits the lowest formation energy of all the defect configurations tested. These molecular bridge defects have been shown to greatly enhance the electron transmission in the out-of-plane direction.[32] All of these observations strongly indicate that the generation of molecular bridges between layers under electrical stress plays an important role in the electron transport across the capacitor.

The relative importance of each defect type cannot be determined solely from the *I-V* data. For example, the data taken at I_{comp} = 100 nA (e.g., Figure 5a) drives the capacitor close to SBD with the generation of a high number of defects, many of which we surmise are molecular bridges. The large change in the conductivity facilitates the observation that an effective thickness must be introduced to fit the data within the Ginestra framework. In contrast, capacitors subjected to a much lower current compliance stress (I_{comp} = 100 pA) generate far fewer defects and show only small increases in conductivity during RVS, as shown in Figure 5d and Figure S5. Such small changes in the *I-V* curves can be modeled in Ginestra equally well by a mix of changes in both effective thickness and trap density, and thus it is not possible even at a qualitative level to estimate the relative importance between defects. A similar conclusion is reached if the RVS ramp rate is varied as shown in Figure S6. Notwithstanding this variability of the RVS curves when the experimental parameters are changed, the data is highly reproducible under fixed conditions. For example, Figure 5c shows that the change in the resistance measured for several capacitors is tightly grouped for a given RVS cycle.

2.4. Analysis of Soft Dielectric Breakdown Using TEM.

Critical physical insight comes from the TEM investigations. Specifically, we use TEM imaging and spectroscopy to study the physical and chemical changes at atomic length scales in h-BN after soft dielectric breakdown. High-resolution TEM (HRTEM) and scanning TEM (STEM) are used for imaging physical changes due to electrical stress, while electron energy loss spectroscopy (EELS) and energy-dispersive X-ray (EDX) spectroscopy are used to identify chemical changes after dielectric breakdown. We use FIB for site-specific sample preparation for the TEM studies. Breakdown is initiated by stressing capacitors *ex situ* by CAFM using a RVS with I_{comp} ∼ 100 nA, as shown in Figure S7a. The stressed capacitor does not show any gross physical damage, as seen in the scanning electron microscopy (SEM) micrograph of Figure S7b. Large area cross-sectional TEM micrographs of the capacitor, Figure S7c, also do not show any structural damage.

It is important to emphasize that the HRTEM data presented here shows h-BN after SBD, i.e., a breakdown path has formed between the electrodes and the resistance is very low. As such, the TEM data shows the aftermath of the

https://doi.org/10.1021/acsaelm.2c01736
ACS Appl. Electron. Mater. 2023, 5, 1262−1276

soft breakdown event and does not necessarily show the defects, e.g., molecular bridges, arising from the electrical stress during the SILC phase. Experiments were attempted in which the stressing was stopped prior to SBD, as in the RVS measurements of Figure 5a,b, but no contrast changes could be observed in any of the TEM micrographs. This can be explained by the relatively large 50−100 nm thickness of the TEM samples in comparison to the subnanometer diameter of the molecular bridges; the bridge defects would not give enough contrast to be visible in cross-sectional TEM micrographs.

Representative TEM data is shown in Figure 6 in which a 10 nm-thick h-BN capacitor of area 500 × 500 nm^2 is subjected to breakdown. The cross-sectional HRTEM micrograph of the stressed capacitor in Figure 6a shows that the crystallinity of the h-BN is severely disrupted compared to the unstressed sample, e.g., Figure 2c. This remarkable micrograph is taken directly at the breakdown spot, where the h-BN layers appear to abruptly terminate over a very narrow region while maintaining crystallinity just nearby. If we assume the breaks in the lattice structure represent the current path, this path is ≪1 nm in width and traverses the capacitor in a zigzag manner (also see Figure S8), the latter also reflecting the fact that charge transport may also be assisted by defects in the plane of the h-BN layers. We cannot rule out the possibility that the breakdown spot itself is larger than ∼1 nm and might not be fully captured because it is entirely fortuitous where the FIB cut transverses the capacitor in the preparation of the TEM sample. Nonetheless, all data indicate that the breakdown spot is nearby given the clearly observable formation of physical defects, reduced crystallinity, and migration of Ti in the h-BN layers (see below). Based on the TEM results, we conclude that the long-range crystalline structure of h-BN is severely disrupted after SBD and that metal migration through the breakdown region leads to the formation of a metallic conducting path, as now discussed.

We further analyze the stressed capacitor shown in Figure 6a using STEM. Physical defects at the bottom Au electrode are observed, as shown in Figure 6b, where a truncated cone-like feature is formed after breakdown. We perform EELS analysis near this truncated cone to analyze the chemical components. A normalized EELS line spectrum of Ti across the capacitor is shown in Figure 6c, which shows the presence of Ti at the bottom Au electrode, indicating the migration of Ti during the breakdown process. Conversely, the unstressed h-BN capacitor does not show any signature of Ti at the bottom electrode, as shown in Figure S9, confirming that Ti migration occurs due to the breakdown. We also confirm the presence of Ti at the bottom Au electrode using EDX analysis of the breakdown site. A STEM micrograph of the breakdown location is shown in Figure 6d where an EDX compositional analysis for Au and Ti is performed and the results are shown in Figure 6e,f, respectively. Signatures of Ti are clearly present at the truncated cone site in the bottom Au electrode.

At present, it is not known whether the migration of metal influences the dielectric degradation process prior to breakdown and more research is required in this direction. Our DFT calculations do indicate that the substitution of boron by Ti is energetically favorable at boron monovacancy defects (with a low formation energy E_{form} = 7.10 eV), and the resulting band structure of Ti/h-BN is completely metalized. In comparison, substitution of Ti into a nitrogen monovacancy is far less favorable (with E_{form} = 19.47 eV). Thus, the generation of boron vacancies coupled with metal diffusion under electrical stress could promote the migration of Ti inside the bulk h-BN, with the generation of metalized Ti/h-BN defects giving rise to electrical shorting between layers. There is no experimental evidence for this conjecture at present as we do not observe any Ti in the bulk h-BN regions. However, as noted above for molecular bridge structures, stress-induced defects may simply be extremely difficult to directly observe in TEM. Furthermore, migration of metal ions to and from the electrodes has been proposed as a possible mechanism for the related phenomenon of resistive switching in h-BN for resistive random access memory (ReRAM) devices.[43] For future experiments, we suggest exploring different electrode materials with varying diffusion coefficients (e.g., graphene, Pt, Ag, Cu) to assess the influence of metal migration on the defect generation and overall breakdown process.

2.5. *Ab Initio* Studies of Stress Induced Defects. The Ginestra simulations show the typical density of traps during the initial SILC phase of dielectric degradation is of the order of ∼5 × 10^{17} cm^{-3}. This translates to ∼1000 traps being present in a typical capacitor of 1 × 1 μm^2 area with 10 nm-thick h-BN, or ∼30 defects per h-BN layer. This low density makes individual defects extremely challenging to locate even using atomic resolution experimental techniques such as TEM. We have therefore undertaken DFT calculations to elucidate the possible defect configurations, which could contribute to the h-BN degradation in agreement with our experimental findings. The results from the previous DFT studies of defects in electrically stressed h-BN are also incorporated.[31,32]

Early DFT studies highlighted the possible existence of a large pool of defects in h-BN.[44,45] Two of the simplest intrinsic structural defects in h-BN are nitrogen and boron monovacancies, with more complex structures possible including di- and trivacancies of boron and nitrogen, metal complexes, and permutations of these defects. Extrinsic defects from trace impurities and the growth environment, e.g., oxygen and carbon, have also been reported, which could exist either as an interstitial defect or form substitutional defects in the h-BN crystal. Since we are studying monocrystalline h-BN, such extrinsic defects do not have to be considered here.

The large library of possible defects in h-BN makes it challenging to uniquely identify the defects associated with the various stages of the breakdown. In our DFT studies, we focus on defects in h-BN, which qualitatively describe charge transport in the out-of-plane direction, which is most relevant to breakdown across a capacitor stack. We find that when two atomic defects are aligned in adjacent layers of h-BN, the resulting overall defect structure can significantly increase the orbital overlap between adjacent h-BN layers and in several cases lead to strong bonding between the two layers. Such defects have been termed molecular bridges by Strand *et al.*[31] and our DFT results reveal three bridge structures corresponding to the lowest formation energies among all structures considered in our study. As such, we postulate that the generation of such molecular bridge defects contribute significantly to the observed out-of-plane charge transfer and electrical shorting between layers, an assumption supported by the electronic transmission calculations of Ducry *et al.*[32] The presence of such molecular bridges across the van der Waals gap between adjacent h-BN layers thus provides charge transport 'highways' that facilitate vertical current flow across the h-BN stack. We cannot fully confirm yet whether the three bridge structures are indeed the lowest energetically among all

https://doi.org/10.1021/acsaelm.2c01736
ACS Appl. Electron. Mater. 2023, 5, 1262−1276

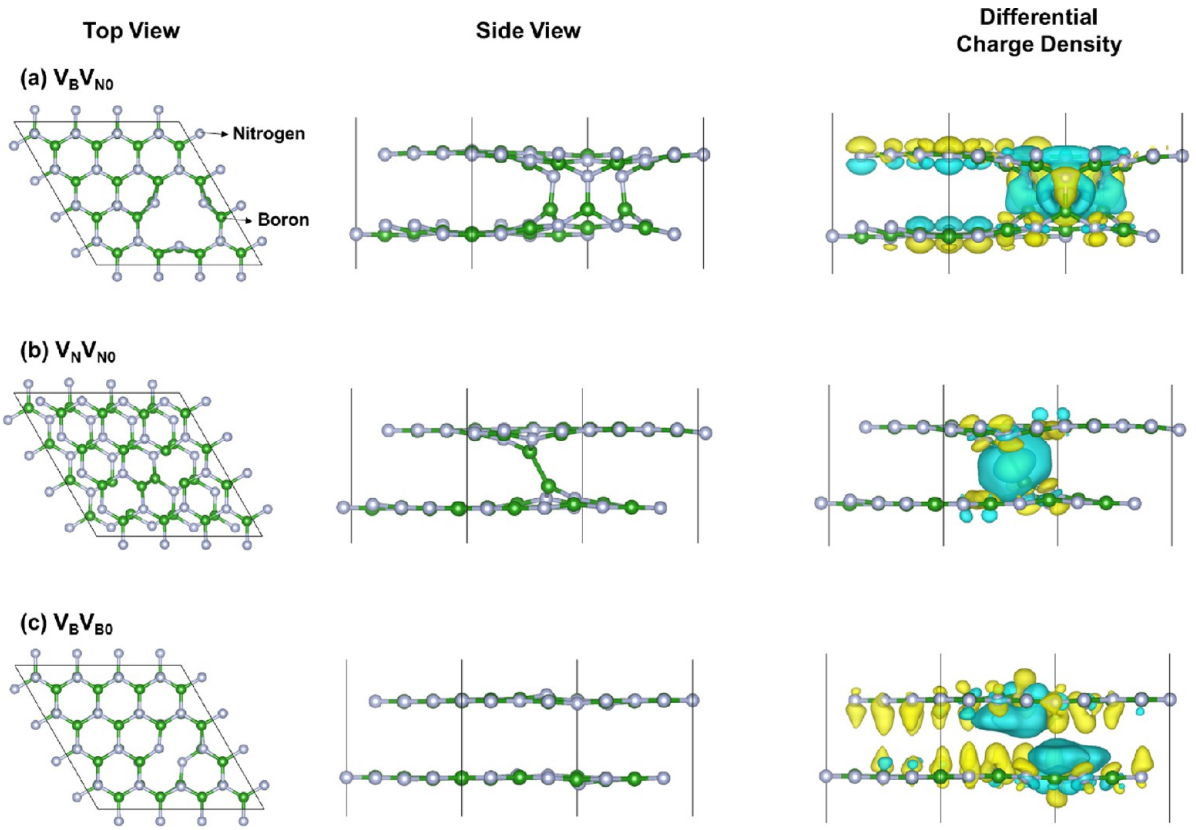

Figure 7. Top view, side view, and differential charge density map for defect structures of (a) V_BV_{N0}, (b) V_NV_{N0}, and (c) V_BV_{B0}. Green and white balls represent boron and nitrogen atoms, respectively. Only three defect configurations have been shown here and a complete list of defects is shown in Figure S10. The various possible combinations of defect structures have been calculated considering the presence of both boron (V_B) and nitrogen (V_N) monovacancies in the adjacent layers of a bilayer h-BN. The numerical subscript in the defect nomenclature indicates the spatial location of the defect in the bottom layer of h-BN compared to the adjacent top layer. Molecular bridges are formed between the adjacent h-BN layers for V_BV_{N0} and V_NV_{N0} defects. The differential charge density map has been overlapped on the side view atomic structure to show the extent of charge overlap. Here, yellow sections represent electron accumulation while cyan sections represent electron depletion. Note that not all the defect configurations result in a molecular bridge, e.g., the V_BV_{B0} defect in panel (c).

possible defect configurations and charge states, but other defect pairs tend to have much larger formation energy and hence while they may contribute to the charge transfer, these non-bridging defects are presumably smaller in number.

In our DFT calculations, we present cases where two monovacancies of boron (V_B) and/or nitrogen (V_N) are aligned in AB stacked bilayer h-BN. The nature of these configurations could also be termed "defect clustering", and clustering has been shown in conventional dielectrics,[46] such as HfO_2, to significantly affect the defect generation rate, i.e., it is more energetically favorable to create a new defect near a pre-existing defect. In the case of h-BN, the spatial proximity to a pre-existing V_N (or V_B) defect significantly reduces E_{form} for the generation of a subsequent V_B (or V_N) defect. A representative example showing a top view of the resulting defect structure is shown in Figure 7a, where a V_B defect is present in the first layer and a V_N defect is located directly below it in the second layer. We label this defect configuration V_B-V_{N0}. The numerical subscript "0" indicates that the position of V_N in the second h-BN layer is directly below V_B in the first layer. This spatial arrangement of defects results in slight distortion of the h-BN crystal at the defect site and three localized B−N bonds are formed between layers, as shown in the side-view representation. The resulting overall defect structure shows a large overlap of charge density across the h-BN layers, creating charge pockets, which can presumably support high charge transmission between the layers, as noted by Ducry *et al.*[32] The existence of a molecular bridge strongly suggests that this type of generated defect is linked to electrical shorting between layers in the breakdown measurements. In fact, the band structure calculations of defective few-layer h-BN show the existence of multiple localized defect levels created around the Fermi level, which may serve as electronic states to mediate hopping conduction across the vertical direction of the h-BN stacks. Another example of a defect configuration is where two V_N defects are aligned in adjacent layers, as shown in Figure 7b. This defect configuration is labeled as V_N-V_{N0}. The side view of the resulting overall defect structure shows that a single N−N bond is created at the defect site, resulting in a localized overlap of charge density cloud. As above, the molecular bridges formed between the adjacent h-BN layers most likely lead to electrical shorting between layers.

Not all the interlayer vacancy defect configurations result in a molecular bridge. An example is shown in Figure 7c where two V_B defects are present in adjacent h-BN layers. The resulting overall defect V_B-V_{B0} does not form any bond between the layers and the extent of charge overlap is significantly reduced compared to the V_B-V_{N0} and V_N-V_{N0} defects.

We also consider alternative defect configurations in which the defect in one layer is laterally positioned one to two lattices spacing away from a defect in the adjacent layer. Including

https://doi.org/10.1021/acsaelm.2c01736
ACS Appl. Electron. Mater. 2023, 5, 1262−1276

defects that are aligned between adjacent layers, this generates a total of 9 defect combinations (V_BV_{N0}, V_BV_{N1}, V_BV_{N2}, V_NV_{N0}, V_NV_{N1}, V_NV_{N2}, V_BV_{B0}, V_BV_{B1}, and V_BV_{B2}). The formation energy (E_{form}) of all 9 defect configurations is shown in Table S4, and the resulting overall defect structures are shown in Figures S10. Some of the key findings are as follows: (i) The molecular bridge defect V_BV_{N0} has the minimum E_{form} among all the defects considered here. (ii) The three most energetically favorable defects V_BV_{N0} (E_{form} = 12.42 eV), V_BV_{N1} (E_{form} = 16.73 eV), and V_NV_{N0} (E_{form} = 17.24 eV) all induce molecular bridges with varying number of bonds and are likely to be responsible for electrical shorting. (iii) Two of the defects (V_NV_{N1} and V_NV_{N2}) show substantial charge density overlap without the creation of a molecular bridge, a result which demonstrates that although the formation of this defect is far less likely than the molecular bridge defects (the formation energy is at least 2 eV higher), charge transfer may occur and contribute to the leakage current if such defects are generated in sufficient numbers.

3. DISCUSSION

3.1. General Characteristics of Degradation in Electrically Stressed h-BN. The TDDB trend shown in Figure 4 qualitatively resembles conventional bulk gate dielectrics (e.g., SiO_2 and HfO_2), and similar stages of dielectric degradation resulting from defect generation are identifiable, including charge trapping, SILC, and soft breakdown. The breakdown field strength measured for h-BN is $\xi_{BD} \sim 15$ MV/cm, which is comparable or higher than conventional gate dielectric films, e.g., ~13 MV/cm for SiO_2. Ginestra simulation employing a trap-assisted tunneling defect mechanism has been extensively applied to model charge transport in bulk gate dielectrics in the past, and we find the model framework works equally well for h-BN. Simulation fittings to the experimental *I-V* data provide a value of the defect density in crystalline h-BN of the order of 10^{17}–10^{18} cm^{-3}. This is less than the intrinsic defect density in HfO_2 (~5×10^{18} to 5×10^{19} cm^{-3}), although orders of magnitude higher compared to thick CMOS-quality SiO_2 (~10^{15} cm^{-3}) films. The higher defect density in h-BN compared to SiO_2 may be intrinsic (i.e., pre-existing) but could also arise from defects induced by the top electrode deposition observed in the TEM micrographs, e.g., Figure 2c. Creating an ideal, i.e., clean and defect-free, electrical contact on a 2D crystalline material is a commonly encountered process challenge,[47,48] and research efforts are ongoing to tackle this problem.

However, one marked difference in the Ginestra simulation of h-BN is that in addition to simply increasing the trap density, which is typically the case when modeling the onset of breakdown in HfO_2 and SiO_2, a change in effective thickness of the film had to be incorporated to correctly model the breakdown *I-V* data for h-BN. We attribute this difference to the presence of an alternative defect generation mechanism arising from the h-BN layering, namely, the formation of molecular bridges, which effectively connect two adjacent layers locally at the defect site. DFT calculations show that for two monovacancies in adjacent h-BN layers, at least three of the defect configurations (V_BV_{N0}, V_BV_{N1}, and V_NV_{N0}) result in bridge formations, which also exhibit the lowest formation energies of all the defect combinations considered. Strand *et al.*[31] have also shown that such a molecular bridge can extend to more than two h-BN layers. Linking DFT with electronic transmission calculations, Ducry *et al.*[32] showed that bridging defects can lead to a large increase in charge transmission between adjacent layers in comparison to the much higher resistance of alternative current flow paths. This suggest that the bridging defects give rise to a large change in resistance in the out-of-plane direction corresponding to one monolayer thickness. We have previously observed this effect directly in highly localized CAFM experiments[13] showing the breakdown of individual h-BN layers and called such events "electrical shorting" between the layers.

Other classes of defects can also nucleate, all of which may contribute with varying extent to the increase in leakage current on stressing, in particular those defects with large overlap between the charge density clouds, e.g., V_NV_{N1} and V_NV_{N2}, as shown in Figure S10 and Table S4. However, we note that all other defects considered in the DFT calculations have much higher formation energy than the V_BV_{N0}, V_BV_{N1}, and V_NV_{N0} molecular bridge defects.

3.2. Physical Removal of h-BN Is Not Intrinsic to Breakdown. The physical removal of h-BN has been observed previously during breakdown by CAFM and has been interpreted as the basis for a "layer-by-layer" breakdown mechanism in h-BN.[10] We argue that the physical removal of material is not an intrinsic mechanism of breakdown in h-BN but rather a manifestation of hard breakdown, i.e., breakdown under very high current density conditions. We have shown in our previous works using CAFM that a dielectric breakdown in h-BN is not always accompanied by physical removal of h-BN at the breakdown site.[13,14,25] The general conclusion from CAFM is that the removal of h-BN material does not occur at very low current compliance but is frequent for hard breakdown as a large amount of energy is released. Such scenarios are not uncommon in conventional gate dielectrics as well, where destructive material damage is observed during hard breakdown of devices, whereas physical and structural changes become less frequent under soft breakdown conditions (which is of most concern in the context of device reliability for realistic use). This has also been discussed in a recent molecular dynamics (MD) study, which highlighted that both swelling and material removal can be expected in multi-layer h-BN subjected to high electron injection.[49]

However, we note that both the MD simulations and the CAFM measurements[10] provide data taken when the h-BN is not capped with an electrode. For practical applications in electronic devices, the h-BN is always capped with an electrode, as in the experiments presented here. In this situation, hard breakdown can lead to material removal and physical destruction of the capacitor. In contrast under SBD conditions, it is difficult to envision how h-BN layers can be removed from underneath a metal electrode. Compelling evidence is provided by the TEM micrographs taken precisely at the breakdown path formed by the SBD event, e.g., Figure 6a; the h-BN layers are disrupted by the breakdown event, but clearly no gross removal of material occurs. This assertion is further supported by our AFM observations in which most capacitors show no indication of material removal after being subjected to SBD stressing. For example, out of 35 capacitors measured on a 12 nm flake, only 2 capacitors showed the removal of h-BN when stressed to typical SBD conditions of I_{comp} = 100 nA; but the material removal itself was catastrophic and destructive for both capacitors, indicating that hard, not soft, breakdown must have occurred in these two cases. Note that a distribution in the breakdown hardness is expected, even

https://doi.org/10.1021/acsaelm.2c01736
ACS Appl. Electron. Mater. 2023, 5, 1262−1276

for a fixed I_{comp} because the breakdown event is statistical in nature, as observed, for example, in SiO_2 gate oxides.[50]

4. CONCLUSIONS

In this work, we have carried out a study on the reliability of monocrystalline h-BN for potential application in gate dielectrics. Our results highlight that h-BN shares many similarities with the breakdown observed in conventional SiO_2 and HfO_2 gate dielectrics, including the existence of charge trapping, SILC, and SBD stages. Based on the electrical measurements of ~1 × 1 μm^2 capacitor test structures, charge transport modeling, and TEM analysis, we propose an atomic-scale picture of degradation and breakdown in h-BN. The stress-induced increase in leakage current may arise from the generation of many different types of defects. However, DFT calculations[31,32] show that three defect pairs in particular created from adjacent boron and nitrogen monovacancies (labeled V_BV_{N0}, V_BV_{N1}, and V_NV_{N0}) have the lowest formation energy. Moreover, these three defects form molecular bridges between two adjacent layers, which effectively "electrically shorts" the two layers at the defect location, thereby resulting in a substantial increase in the out-of-plane leakage current. An alternative breakdown mechanism, the physical removal of h-BN material, most likely only occurs under hard breakdown conditions. Direct TEM imaging of the nanoscale breakdown location shows that SBD in h-BN leads to reduced crystallinity and migration of Ti through only a narrow leakage path, with no gross material removal.

The significance of metal (Ti) migration to the breakdown process itself is not understood at present and requires further study. This highlights a rather general problem, which is to directly confirm the major defects responsible for the degradation under stressing. Our DFT calculations suggest a wide range of defects in h-BN including point defects (e.g., vacancies and interstitials) as well as defect aggregates (e.g., molecular bridges, multivacancy defects). Many of these defects have multiple charge states, which further complicates the analysis. Future studies require complementing the *ab initio* calculations with *in situ* (S)TEM measurements to elucidate the physical structure of these defects, the substitutional metal defects if present, and their contribution in the breakdown process. Finally, it is noteworthy that such research is also of importance in understanding the switching mechanism in proposed h-BN-based ReRAM technology.[32]

5. EXPERIMENTAL SECTION

5.1. Device Fabrication. Pre-patterned SiO_2 (300 nm)/Si substrates were cleaned in acetone, IPA, and DI water and then dried in N_2 prior to deposition of the bottom electrode. The bottom electrode is a 3 nm Ti adhesion layer and 30 nm Au layer deposited sequentially using sputtering without breaking the vacuum. Single crystal h-BN was purchased from HQ Graphene. The h-BN flakes were exfoliated on polydimethylsiloxane (PDMS) film using blue Nitto tape, and a PDMS stamp was used to transfer the flakes onto the Ti-Au coated Si substrates. The h-BN sample was then annealed in high vacuum at 300 °C for ~3−4 h to remove organic residues. Thin h-BN flakes were identified using a combination of an optical microscope and AFM imaging in tapping mode. Either a JPK Nanowizard 3 or a Bruker Dimension Icon AFM were used for imaging. Once suitable h-BN flakes were found, the top electrodes were defined on the flakes using electron beam lithography, with the active electrode area varying between 500 nm × 500 nm and 3 μm × 3 μm. The top electrode consisting of 7 nm Ti and a capping layer of 30 nm Au was deposited sequentially using an electron beam evaporator. The samples were left in acetone overnight at 60 °C for the resist lift-off. The sample was vacuum dried at 100 °C for 5−6 h prior to CAFM electrical measurements.

5.2. Conduction Atomic Force Microscopy. All the CAFM measurements in this work were carried out using a JPK Nanowizard 3 AFM. For CAFM, Pt wire levers (RMN25Pt300B, Rocky Mountain, k_c = 18 N/m) were used because these all-metal levers do not suffer from wear of the conducting material from the tip apex. We used a combination of tapping mode imaging to first identify the individual capacitors followed by switching to contact mode on top of the capacitors to carry out electrical measurements. All the electrical measurements shown in this work are carried out in contact mode at an applied force of 10−40 nN for the entire duration of the measurement. A semiconductor parameter analyzer (Keithley 4200) was externally configured with the AFM (bias is applied to the AFM tip; the sample is electrically grounded) allowing us to measure the leakage current (ranging from pA to mA) and also to limit the current flow through the capacitor at the instant of the dielectric breakdown. A suite of electrical measurements including RVS, CVS, and constant current injection was used.

It is important to be aware of tip contamination during CAFM measurements, which leads to variability in the measured current and possible loss of electrical conductivity over time. Appropriate measures should be taken to mitigate such effects. Here, all CAFM tips were pre-cleaned in oxygen plasma for 3 min prior to measurements to remove organic residues. The CAFM experiments were carried out under a continuous flow of nitrogen to maintain the relative humidity at ~15% and avoid the formation of a water meniscus at the tip apex, which is detrimental to localized electrical measurement. During experiments, the tip is occasionally moved to the nearby Ti-Au bottom electrode surface and an *I-V* measurement is taken to check the electrical integrity of the tip, with an ohmic *I-V* of low resistance indicating that the tip is suitably conducting for CAFM measurements to continue.

Note that a thermal drift of the tip with respect to the surface (typically of order ~1 nm/s) is not an issue because the CAFM experiments are undertaken with the tip always in contact with the capacitor electrode. It is of no consequence to the electrical measurement if the tip slowly drifts over the electrode area. The ability to monitor over long time scales, essential in experiments such as TDDB, is another advantage of the Cap-AFM approach.

Standard tapping mode AFM was also used to obtain high-resolution topography images of the h-BN flakes and capacitors both before and after the electrical measurements using sharp non-conducting cantilevers (Ultra-sharp Si levers, Tap 190G, Budget-Sensors, k_c = 48 N/m).

5.3. Transmission Electron Microscopy. Cross-section samples for the TEM analysis are prepared by FIB milling in a FEI dual-beam Helios 600i system. A few micron-thick SiO_x is deposited first at low temperature, which is followed by a 5 μm-thick sacrificial Pt layer. Ga ion beam milling is then used to prepare TEM cross-sectional lamella of the capacitors. The lamella is ~12 μm long and ~50−100 nm thick. During ion milling, the acceleration voltage is dropped from 25 to 5 kV for the polishing step to remove most of the amorphous layers on the sample surface. Final polishing was carried out in a Fischione 1040 NanoMill at 900 V for 5 min. The design of our test structures allows us to prepare cross-sectional TEM lamellae of multiple capacitors in a single experiment, thereby increasing the efficiency of the sample preparation. The structural analysis of the sample is carried out using a FEI Titan microscope and JEOL JEM 2200FS operating at 200 kV. The images were acquired in conventional TEM imaging mode under parallel illumination. EDX analysis is also carried out on the JEOL JEM 2200FS in STEM mode.

5.4. DFT Calculations. Theoretical calculations were carried out by using the Vienna *ab initio* simulation package (VASP)[51,52] with generalized gradient approximation (GGA) with the Perdew−Burke−Ernzerhof (PBE)[53] functional. For valence electrons, a plane-wave basis set was adopted with an energy cutoff of 500 eV and the ionic cores were described with the projector augmented-wave method. A common approach to account for van der Waals interactions is to

https://doi.org/10.1021/acsaelm.2c01736
ACS Appl. Electron. Mater. 2023, 5, 1262−1276

include a DFT-D3[54] correction as proposed by PBE.[53] The optimized lattice parameter for a h-BN monolayer was calculated to be 2.50 Å, which employed an energy criterion of 10^{-8} eV reached for a self-consistency cycle and the residual forces having converged to less than 0.001 eV $Å^{-1}$. For the optimization of all the relaxation atoms, a 4 × 4 supercell h-BN is constructed as a substrate where 19 × 19 × 1 Monkhorst−Pack k-point grids were used to sample the Brillouin zone. In addition, to avoid the interlayer interactions, a vacuum spacing in the z direction was set to be 15 Å.

5.5. Charge Transport Modeling. Charge transport through the considered material stack is modeled accounting simultaneously for a variety of charge transport mechanisms, such as direct/Fowler−Nordheim tunneling, trap assisted tunneling (TAT), drift-diffusion in conduction/valence and defect bands, thermionic emissions (the dominant one depends on the external conditions − temperature and voltage − as well as on the device state). Defects are treated as discrete entities described through two key parameters, the thermal ionization (E_T) and relaxation (E_{REL}) energies, that identify their specific atomic structure.[35,55] Trap capture and emission times are calculated in the framework of the multi-phonon theory accounting for carrier−phonon coupling and lattice relaxation processes.[35,56−58] An extended description of the charge transport models is reported in prior works.[35,59] Charge transport equations are self-consistently solved together with Poisson's equation, accounting for defect charge state and occupation probability. Further details of the modeling are provided in Note S1 "An outline of the Ginestra platform" in the Supporting Information.

■ ASSOCIATED CONTENT

Supporting Information

The Supporting Information is available free of charge at https://pubs.acs.org/doi/10.1021/acsaelm.2c01736.

TEM micrographs of the as-prepared and electrically biased h-BN capacitors, *I-V* curves along with simulation fittings, DFT calculations of various interplanar defects in h-BN, and description of the charge transport simulations (PDF)

■ AUTHOR INFORMATION

Corresponding Authors

Alok Ranjan − *Division of Nano-and-Bio Physics, Department of Physics, Chalmers University of Technology, Gothenburg 41296, Sweden; Engineering Product Development, Singapore University of Technology and Design, Singapore 487372, Singapore;* orcid.org/0000-0003-4592-1674; Email: alok.ranjan@chalmers.se

Sean J. O'Shea − *Agency for Science Technology and Research, Institute of Materials Research and Engineering, Singapore 138634, Singapore;* orcid.org/0000-0003-0385-6245; Email: s-oshea@imre.a-star.edu.sg

Authors

Andrea Padovani − *Dipartimento di Ingegneria Enzo Ferrari, University of Modena and Reggio Emilia, Modena 41125, Italy*

Tong Su − *Science, Mathematics and Technology, Singapore University of Technology and Design, Singapore 487372, Singapore*

Paolo La Torraca − *Dipartimento di Scienze e Metodi dell'Ingegneria, University of Modena and Reggio Emilia, Reggio Emilia 41125, Italy;* orcid.org/0000-0003-4852-4623

Yee Sin Ang − *Science, Mathematics and Technology, Singapore University of Technology and Design, Singapore 487372, Singapore;* orcid.org/0000-0002-1637-1610

Manveer Singh Munde − *Materials Science Centre and Department of Physics, Philipps University Marburg, Marburg 35032, Germany*

Chenhui Zhang − *Physical Science and Engineering Division, King Abdullah University of Science and Technology, Thuwal 23955-6900, Saudi Arabia*

Xixiang Zhang − *Physical Science and Engineering Division, King Abdullah University of Science and Technology, Thuwal 23955-6900, Saudi Arabia;* orcid.org/0000-0002-3478-6414

Michel Bosman − *Agency for Science Technology and Research, Institute of Materials Research and Engineering, Singapore 138634, Singapore; Department of Material Science and Engineering, National University of Singapore, Singapore 117575, Singapore;* orcid.org/0000-0002-8717-7655

Nagarajan Raghavan − *Engineering Product Development, Singapore University of Technology and Design, Singapore 487372, Singapore;* orcid.org/0000-0001-6735-3108

Kin Leong Pey − *Engineering Product Development, Singapore University of Technology and Design, Singapore 487372, Singapore;* orcid.org/0000-0002-0066-091X

Complete contact information is available at: https://pubs.acs.org/10.1021/acsaelm.2c01736

Notes

The authors declare no competing financial interest.

■ REFERENCES

(1) Roy, S.; Zhang, X.; Puthirath, A. B.; Meiyazhagan, A.; Bhattacharyya, S.; Rahman, M. M.; Babu, G.; Susarla, S.; Saju, S. K.; Tran, M. K.; Sassi, L. M.; Saadi, M. A. S. R.; Lai, J.; Sahin, O.; Sajadi, S. M.; Dharmarajan, B.; Salpekar, D.; Chakingal, N.; Baburaj, A.; Shuai, X.; Adumbumkulath, A.; Miller, K. A.; Gayle, J. M.; Ajnsztajn, A.; Prasankumar, T.; Harikrishnan, V. V. J.; Ojha, V.; Kannan, H.; Khater, A. Z.; Zhu, Z.; Iyengar, S. A.; Autreto, P. A.; Oliveira, E. F.; Gao, G.; Birdwell, A. G.; Neupane, M. R.; Ivanov, T. G.; Taha-Tijerina, J.; Yadav, R. M.; Arepalli, S.; Vajtai, R.; Ajayan, P. M. Structure, Properties and Applications of Two-Dimensional Hexagonal Boron Nitride. *Adv. Mater.* **2021**, *33*, No. 2101589.

(2) Dean, C. R.; Young, A. F.; Meric, I.; Lee, C.; Wang, L.; Sorgenfrei, S.; Watanabe, K.; Taniguchi, T.; Kim, P.; Shepard, K. L.; Hone, J. Boron nitride substrates for high-quality graphene electronics. *Nat. Nanotechnol.* **2010**, *5*, 722−726.

(3) Grosso, G.; Moon, H.; Lienhard, B.; Ali, S.; Efetov, D. K.; Furchi, M. M.; Jarillo-Herrero, P.; Ford, M. J.; Aharonovich, I.; Englund, D. Tunable and high-purity room temperature single-photon emission from atomic defects in hexagonal boron nitride. *Nat. Commun.* **2017**, *8*, 705.

(4) Lee, G.-H.; Yu, Y.-J.; Lee, C.; Dean, C.; Shepard, K. L.; Kim, P.; Hone, J. Electron tunneling through atomically flat and ultrathin hexagonal boron nitride. *Appl. Phys. Lett.* **2011**, *99*, 243114.

(5) Fallahazad, B.; Kim, S.; Colombo, L.; Tutuc, E. Dielectric thickness dependence of carrier mobility in graphene with HfO2 top dielectric. *Appl. Phys. Lett.* **2010**, *97*, 123105.

(6) Li, T.; Tu, T.; Sun, Y.; Fu, H.; Yu, J.; Xing, L.; Wang, Z.; Wang, H.; Jia, R.; Wu, J.; Tan, C.; Liang, Y.; Zhang, Y.; Zhang, C.; Dai, Y.; Qiu, C.; Li, M.; Huang, R.; Jiao, L.; Lai, K.; Yan, B.; Gao, P.; Peng, H. A native oxide high-κ gate dielectric for two-dimensional electronics. *Nature Electronics* **2020**, *3*, 473−478.

(7) Maruvada, A.; Shubhakar, K.; Raghavan, N.; Pey, K. L.; O'Shea, S. J. Dielectric breakdown of 2D muscovite mica. *Sci. Rep.* **2022**, *12*, 14076.

(8) Jin, T.; Zheng, Y.; Gao, J.; Wang, Y.; Li, E.; Chen, H.; Pan, X.; Lin, M.; Chen, W. Controlling Native Oxidation of HfS2 for 2D

Materials Based Flash Memory and Artificial Synapse. *ACS Appl. Mater. Interfaces* **2021**, DOI: 10.1021/acsami.0c22561.
(9) Zheng, X.; Wei, Y.; Deng, C.; Huang, H.; Yu, Y.; Wang, G.; Peng, G.; Zhu, Z.; Zhang, Y.; Jiang, T.; Qin, S.; Zhang, R.; Zhang, X. Controlled Layer-by-Layer Oxidation of MoTe2 via O3 Exposure. *ACS Appl. Mater. Interfaces* **2018**, *10*, 30045−30050.
(10) Hattori, Y.; Taniguchi, T.; Watanabe, K.; Nagashio, K. Layer by layer dielectric breakdown of hexagonal boron nitride. *ACS Nano* **2015**, *9*, 916−921.
(11) Palumbo, F.; Liang, X.; Yuan, B.; Shi, Y.; Hui, F.; Villena, M. A.; Lanza, M. Bimodal Dielectric Breakdown in Electronic Devices Using Chemical Vapor Deposited Hexagonal Boron Nitride as Dielectric. *Adv. Electron. Mater.* **2018**, 1700506-n/a.
(12) Britnell, L.; Gorbachev, R. V.; Jalil, R.; Belle, B. D.; Schedin, F.; Katsnelson, M. I.; Eaves, L.; Morozov, S. V.; Mayorov, A. S.; Peres, N. M. R.; Castro Neto, A. H.; Leist, J.; Geim, A. K.; Ponomarenko, L. A.; Novoselov, K. S. Electron tunneling through ultrathin boron nitride crystalline barriers. *Nano Lett.* **2012**, *12*, 1707−1710.
(13) Ranjan, A.; Raghavan, N.; Holwill, M.; Watanabe, K.; Taniguchi, T.; Novoselov, K. S.; Pey, K. L.; O'Shea, S. J. Dielectric Breakdown in Single-Crystal Hexagonal Boron Nitride. *ACS Appl. Electron. Mater.* **2021**, *3*, 3547−3554.
(14) Ranjan, A.; O'Shea, S. J.; Bosman, M.; Raghavan, N.; Pey, K. L. Localized probing of dielectric breakdown in multilayer hexagonal boron nitride. *ACS Appl. Mater. Interfaces* **2020**, *12*, 55000−55010.
(15) Hattori, Y.; Taniguchi, T.; Watanabe, K.; Nagashio, K. Anisotropic dielectric breakdown strength of single crystal hexagonal boron nitride. *ACS Appl. Mater. Interfaces* **2016**, *8*, 27877−27884.
(16) Jiang, L.; Shi, Y.; Hui, F.; Tang, K.; Wu, Q.; Pan, C.; Jing, X.; Uppal, H.; Palumbo, F.; Lu, G.; Wu, T.; Wang, H.; Villena, M. A.; Xie, X.; McIntyre, P. C.; Lanza, M. Dielectric breakdown in chemical vapor deposited hexagonal boron nitride. *ACS Appl. Mater. Interfaces* **2017**, *9*, 39758−39770.
(17) Palumbo, F.; Wen, C.; Lombardo, S.; Pazos, S.; Aguirre, F.; Eizenberg, M.; Hui, F.; Lanza, M. A Review on Dielectric Breakdown in Thin Dielectrics: Silicon Dioxide, High-k, and Layered Dielectrics. *Adv. Funct. Mater.* **2020**, *30*, No. 1900657.
(18) Cui, Z.; He, Y.; Tian, H.; Khanaki, A.; Xu, L.; Shi, W.; Liu, J. Study of Direct Tunneling and Dielectric Breakdown in Molecular Beam Epitaxial Hexagonal Boron Nitride Monolayers Using Metal−Insulator−Metal Devices. *ACS Appl. Electron. Mater.* **2020**, *2*, 747−755.
(19) Chandni, U.; Watanabe, K.; Taniguchi, T.; Eisenstein, J. P. Evidence for defect-mediated tunneling in hexagonal boron nitride based junctions. *Nano Lett.* **2015**, *15*, 7329−7333.
(20) Ji, Y.; Pan, C.; Zhang, M.; Long, S.; Lian, X.; Miao, F.; Hui, F.; Shi, Y.; Larcher, L.; Wu, E.; Lanza, M. Boron nitride as two dimensional dielectric: Reliability and dielectric breakdown. *Appl. Phys. Lett.* **2016**, *108*, No. 012905.
(21) Hui, F.; Fang, W.; Leong, W. S.; Kpulun, T.; Wang, H.; Yang, H. Y.; Villena, M. A.; Harris, G.; Kong, J.; Lanza, M. Electrical Homogeneity of Large-Area Chemical Vapor Deposited Multilayer Hexagonal Boron Nitride Sheets. *ACS Appl. Mater. Interfaces* **2017**, *9*, 39895−39900.
(22) Watanabe, K.; Taniguchi, T.; Kanda, H. Direct-bandgap properties and evidence for ultraviolet lasing of hexagonal boron nitride single crystal. *Nat. Mater.* **2004**, *3*, 404−409.
(23) Greenaway, M. T.; Vdovin, E. E.; Ghazaryan, D.; Misra, A.; Mishchenko, A.; Cao, Y.; Wang, Z.; Wallbank, J. R.; Holwill, M.; Khanin, Y. N.; Morozov, S. V.; Watanabe, K.; Taniguchi, T.; Makarovsky, O.; Fromhold, T. M.; Patanè, A.; Geim, A. K.; Falko, V. I.; Novoselov, K. S.; Eaves, L. Tunnel spectroscopy of localised electronic states in hexagonal boron nitride. *Commun. Phys.* **2018**, *1*, 94.
(24) Ranjan, A.; Puglisi, F. M.; Raghavan, N.; O'Shea, S. J.; Shubhakar, K.; Pavan, P.; Padovani, A.; Larcher, L.; Pey, K. L. Random Telegraph Noise in 2D Hexagonal Boron Nitride Dielectric Films. *Appl. Phys. Lett.* **2018**, *112*, 133505.
(25) Ranjan, A.; Raghavan, N.; O'shea, S. J.; Mei, S.; Bosman, M.; Shubhakar, K.; Pey, K. L. Conductive Atomic Force Microscope Study of Bipolar and Threshold Resistive Switching in 2D Hexagonal Boron Nitride Films. *Sci. Rep.* **2018**, *8*, 1−9.
(26) Hattori, Y.; Taniguchi, T.; Watanabe, K.; Nagashio, K. Determination of Carrier Polarity in Fowler-Nordheim Tunneling and Evidence of Fermi Level Pinning at the Hexagonal Boron Nitride/Metal Interface. *ACS Appl. Mater. Interfaces* **2018**, 11732.
(27) Hattori, Y.; Taniguchi, T.; Watanabe, K.; Nagashio, K. Comparison of device structures for the dielectric breakdown measurement of hexagonal boron nitride. *Appl. Phys. Lett.* **2016**, *109*, 253111.
(28) Hattori, Y.; Taniguchi, T.; Watanabe, K.; Nagashio, K. Impact ionization and transport properties of hexagonal boron nitride in a constant-voltage measurement. *Phys. Rev. B* **2018**, *97*, No. 045425.
(29) Weir, B. E.; Silverman, P. J.; Alam, M. A.; Baumann, F.; Monroe, D.; Ghetti, A.; Bude, J. D.; Timp, G. L.; Hamad, A.; Oberdick, T. M.; Zhao, N. X.; Ma, Y.; Brown, M. M.; Hwang, D.; Sorsch, T. W.; Madic, J. Gate oxides in 50 nm devices: thickness uniformity improves projected reliability. In *International Electron Devices Meeting 1999. Technical Digest (Cat. No.99CH36318), 5−8 Dec. 1999*, 1999; pp. 437−440, DOI: 10.1109/IEDM.1999.824187.
(30) Kaczer, B.; Degraeve, R.; Groeseneken, G.; Rasras, M.; Kubicek, S.; Vandamme, E.; Badenes, G. Impact of MOSFET oxide breakdown on digital circuit operation and reliability. In *International Electron Devices Meeting 2000. Technical Digest. IEDM (Cat. No.00CH37138), 10−13 Dec. 2000*, 2000; pp. 553−556, DOI: 10.1109/IEDM.2000.904379.
(31) Strand, J.; Larcher, L.; Shluger, A. L. Properties of intrinsic point defects and dimers in hexagonal boron nitride. *J. Phys.: Condens. Matter* **2020**, *32*, No. 055706.
(32) Ducry, F.; Waldhoer, D.; Knobloch, T.; Csontos, M.; Jimenez Olalla, N.; Leuthold, J.; Grasser, T.; Luisier, M. An ab initio study on resistance switching in hexagonal boron nitride. *npj 2D Mater. Appl.* **2022**, *6*, 58.
(33) Roussel, P.; Degraeve, R.; Bosch, C. V. D.; Kaczer, B.; Groeseneken, G. Accurate and robust noise-based trigger algorithm for soft breakdown detection in ultra thin oxides. In *2001 IEEE International Reliability Physics Symposium Proceedings. 39th Annual (Cat. No.00CH37167), 30 April-3 May 2001*, 2001; pp. 386−392, DOI: 10.1109/RELPHY.2001.922931
(34) Smyth, C. M.; Addou, R.; Hinkle, C. L.; Wallace, R. M. Origins of Fermi-Level Pinning between Molybdenum Dichalcogenides (MoSe2, MoTe2) and Bulk Metal Contacts: Interface Chemistry and Band Alignment. *J. Phys. Chem. C* **2019**, *123*, 23919−23930.
(35) Vandelli, L.; Padovani, A.; Larcher, L.; Southwick, R. G.; Knowlton, W. B.; Bersuker, G. A Physical Model of the Temperature Dependence of the Current Through SiO2\HfO2 Stacks. *IEEE Trans. Electron Devices* **2011**, *58*, 2878−2887.
(36) Larcher, L.; Padovani, A.; Vandelli, L. A simulation framework for modeling charge transport and degradation in high-k stacks. *J. Comput. Electron.* **2013**, *12*, 658−665.
(37) Applied Materials, https://www.appliedmaterials.com/us/en/semiconductor/ginestra-software.html (accessed 20230126).
(38) McPherson, J. W. Time dependent dielectric breakdown physics − Models revisited. *Microelectron. Reliab.* **2012**, *52*, 1753−1760.
(39) Young Hee, K.; Onishi, K.; Chang Seok, K.; Hag-Ju, C.; Nieh, R.; Gopalan, S.; Choi, R.; Jeong, H.; Krishnan, S.; Lee, J. C. Area dependence of TDDB characteristics for HfO2 gate dielectrics. *IEEE Electron Device Lett.* **2002**, *23*, 594−596.
(40) Degraeve, R.; Kauerauf, T.; Cho, M.; Zahid, M.; Ragnarsson, L. A.; Brunco, D. P.; Kaczer, B.; Roussel, P.; Gendt, S. D.; Groeseneken, G. Degradation and breakdown of 0.9 nm EOT SiO2/ALD HfO2/metal gate stacks under positive constant voltage stress. In *IEEE International Electron Devices Meeting, 2005. IEDM Technical Digest., 5−5 Dec. 2005*, 2005; pp. 408−411, DOI: 10.1109/IEDM.2005.1609364.

(41) Mannequin, C.; Gonon, P.; Vallée, C.; Latu-Romain, L.; Bsiesy, A.; Grampeix, H.; Salaün, A.; Jousseaume, V. Stress-induced leakage current and trap generation in HfO2 thin films. *J. Appl. Phys.* **2012**, *112*, No. 074103.
(42) Cartier, E.; Kerber, A. Stress-induced leakage current and defect generation in nFETs with HfO2/TiN gate stacks during positive-bias temperature stress. In *2009 IEEE International Reliability Physics Symposium, 26−30 April 2009*, 2009; pp. 486−492, DOI: 10.1109/IRPS.2009.5173301.
(43) Lin, W.; Zhuang, P.; Akinwande, D.; Zhang, X.-A.; Cai, W. Oxygen-assisted synthesis of hBN films for resistive random access memories. *Appl. Phys. Lett.* **2019**, *115*, No. 073101.
(44) Zobelli, A.; Ewels, C. P.; Gloter, A.; Seifert, G. Vacancy migration in hexagonal boron nitride. *Phys. Rev. B* **2007**, *75*, No. 094104.
(45) Sajid, A.; Reimers, J. R.; Ford, M. J. Defect states in hexagonal boron nitride: Assignments of observed properties and prediction of properties relevant to quantum computation. *Phys. Rev. B* **2018**, *97*, No. 064101.
(46) Strand, J.; La Torraca, P.; Padovani, A.; Larcher, L.; Shluger, A. L. Dielectric breakdown in HfO2 dielectrics: Using multiscale modeling to identify the critical physical processes involved in oxide degradation. *J. Appl. Phys.* **2022**, *131*, 234501.
(47) Schulman, D. S.; Arnold, A. J.; Das, S. Contact engineering for 2D materials and devices. *Chem. Soc. Rev.* **2018**, *47*, 3037−3058.
(48) Wang, Y.; Chhowalla, M. Making clean electrical contacts on 2D transition metal dichalcogenides. *Nat. Rev. Phys.* **2022**, *4*, 101−112.
(49) Liu, P.; Pei, Q.-X.; Zhang, Y.-W. Failure modes and mechanisms of layered h-BN under local energy injection. *Sci. Rep.* **2022**, *12*, 11860.
(50) Sune, J.; Wu, E. Y.; Jimenez, D.; Vollertsen, R. P.; Miranda, E. Understanding soft and hard breakdown statistics, prevalence ratios and energy dissipation during breakdown runaway. In *International Electron Devices Meeting. Technical Digest (Cat. No.01CH37224), 2−5 Dec. 2001*, 2001; pp 6.1.1−6. 1.4, DOI: 10.1109/IEDM.2001.979446.
(51) Kresse, G.; Hafner, J. Ab initio molecular dynamics for open-shell transition metals. *Phys. Rev. B* **1993**, *48*, 13115−13118.
(52) Kresse, G.; Hafner, J. Ab initio molecular-dynamics simulation of the liquid-metal–amorphous-semiconductor transition in germanium. *Phys. Rev. B* **1994**, *49*, 14251−14269.
(53) Perdew, J. P.; Burke, K.; Ernzerhof, M. Generalized Gradient Approximation Made Simple. *Phys. Rev. Lett.* **1996**, *77*, 3865−3868.
(54) Grimme, S.; Antony, J.; Ehrlich, S.; Krieg, H. A consistent and accurate ab initio parametrization of density functional dispersion correction (DFT-D) for the 94 elements H-Pu. *J. Chem. Phys.* **2010**, *132*, 154104.
(55) Padovani, A.; Kaczer, B.; Pešić, M.; Belmonte, A.; Popovici, M.; Nyns, L.; Linten, D.; Afanasev, V. V.; Shlyakhov, I.; Lee, Y.; Park, H.; Larcher, L. A Sensitivity Map-Based Approach to Profile Defects in MIM Capacitors From I-V, C-V, and G-V Measurements. *IEEE Trans. Electron Devices* **2019**, *66*, 1892−1898.
(56) Huang, K.; Rhys, A.; Mott, N. F. Theory of light absorption and non-radiative transitions in F-centres. *Proceedings of the Royal Society of London. Series A. Mathematical and Physical Sciences* **1950**, *204*, 406−423.
(57) Henry, C. H.; Lang, D. V. Nonradiative capture and recombination by multiphonon emission in GaAs and GaP. *Phys. Rev. B* **1977**, *15*, 989−1016.
(58) Zhang, M.; Huo, Z.; Yu, Z.; Liu, J.; Liu, M. Unification of three multiphonon trap-assisted tunneling mechanisms. *J. Appl. Phys.* **2011**, *110*, 114108.
(59) Larcher, L.; Padovani, A.; Puglisi, F. M.; Pavan, P. Extracting Atomic Defect Properties From Leakage Current Temperature Dependence. *IEEE Trans. Electron Devices* **2018**, *65*, 5475−5480.

https://doi.org/10.1021/acsaelm.2c01736
ACS Appl. Electron. Mater. 2023, 5, 1262−1276